LETTER

doi:10.1038/nature12421

Microscopic origin of the '0.7-anomaly' in quantum point contacts

Florian Bauer[1,2]*, Jan Heyder[1,2]*, Enrico Schubert[1], David Borowsky[1], Daniela Taubert[1], Benedikt Bruognolo[1,2], Dieter Schuh[3], Werner Wegscheider[4], Jan von Delft[1,2] & Stefan Ludwig[1]

Quantum point contacts are narrow, one-dimensional constrictions usually patterned in a two-dimensional electron system, for example by applying voltages to local gates. The linear conductance of a point contact, when measured as function of its channel width, is quantized[1–3] in units of $G_Q = 2e^2/h$, where e is the electron charge and h is Planck's constant. However, the conductance also has an unexpected shoulder at $\sim 0.7 G_Q$, known as the '0.7-anomaly'[4–12], whose origin is still subject to debate[11–21]. Proposed theoretical explanations have invoked spontaneous spin polarization[4,17], ferromagnetic spin coupling[19], the formation of a quasi-bound state leading to the Kondo effect[13,14], Wigner crystallization[16,20] and various treatments of inelastic scattering[18,21]. However, explicit calculations that fully reproduce the various experimental observations in the regime of the 0.7-anomaly, including the zero-bias peak that typically accompanies it[6,9–11], are still lacking. Here we offer a detailed microscopic explanation for both the 0.7-anomaly and the zero-bias peak: their common origin is a smeared van Hove singularity in the local density of states at the bottom of the lowest one-dimensional subband of the point contact, which causes an anomalous enhancement in the Hartree potential barrier, the magnetic spin susceptibility and the inelastic scattering rate. We find good qualitative agreement between theoretical calculations and experimental results on the dependence of the conductance on gate voltage, magnetic field, temperature, source–drain voltage (including the zero-bias peak) and interaction strength. We also clarify how the low-energy scale governing the 0.7-anomaly depends on gate voltage and interactions. For low energies, we predict and observe Fermi-liquid behaviour similar to that associated with the Kondo effect in quantum dots[22]. At high energies, however, the similarities between the 0.7-anomaly and the Kondo effect end.

In our measurements, we use the multigate layout on the surface of a GaAs/AlGaAs heterostructure shown in Fig. 1a. By suitably tuning the central- and side-gate voltages, V_c and V_s, at a fixed top-gate voltage, V_t, we can use the device to define a short, one-dimensional (1D) channel, containing a smooth, symmetric barrier, in the two-dimensional electron system (2DES) buried in the heterostructure. To describe such a quantum point contact (QPC), we adopt a 1D model with local interactions and a smooth potential barrier. We treat interactions perturbatively, using either second-order perturbation theory[23] (SOPT) or the functional renormalization group[24–26] (FRG) approach (Supplementary Information, sections 7 and 6, respectively). The lowest 1D subband of the device is modelled by

$$\hat{H} = \sum_{j\sigma} \left[E_{j\sigma} \hat{n}_{j\sigma} - \tau_j \left(d^{\dagger}_{j+1\,\sigma} d_{j\sigma} + \text{h.c.} \right) \right] + \sum_j U_j \hat{n}_{j\uparrow} \hat{n}_{j\downarrow} \qquad (1)$$

Here $\hat{n}_{j\sigma} = d^{\dagger}_{j\sigma} d_{j\sigma}$ counts the number of electrons with spin σ (spin up, $\sigma = \uparrow$ or $+$; spin down, $\sigma = \downarrow$ or $-$) at site j of an infinite, tight-binding chain with hopping amplitude τ_j, on-site interaction U_j and potential energy $E_{j\sigma} = E_j - \sigma\tilde{B}/2$ (Supplementary Fig. 8), and 'h.c.' denotes Hermitian conjugate. The Zeeman energy, $\tilde{B} = |g_{el}|\mu_B B$, describes the effect of a uniform external parallel magnetic field B, where μ_B is the Bohr magneton and g_{el} is the effective g factor (<0 in GaAs). (When similar symbols are used for model parameters and experimental parameters, we add tildes to the former to distinguish them from the latter.) We neglect spin–orbit interactions and other orbital effects. The parameters E_j, U_j and τ_j vary smoothly with j and differ from their bulk values, $E_{bulk} = U_{bulk} = 0$ and $\tau_{bulk} = \tau$ (taken as the unit of energy), only within a central constriction region (CCR) of N sites around $j = 0$, representing the QPC. Sites $j < -N/2$ and $j > N/2$ represent two non-interacting leads, each with bandwidth 4τ, chemical potential μ and bulk Fermi energy $\varepsilon_F = 2\tau + \mu$; we choose $\mu = 0$, implying half-filled leads (Fig. 1b). We set U_j to a fixed value, U, for all but the outermost sites of the CCR, where it drops smoothly to zero.

Within the CCR, we define the QPC barrier by specifying the shape of the 'band bottom' as $\omega_j^{min} = E_j - (\tau_{j-1} + \tau_j) - \mu$ (Fig. 1b, solid black line). We choose ω_j^{min} to define a smooth, symmetric barrier within the CCR, parabolic near the top[3], where we parameterize it as $\omega_j^{min} \approx \tilde{V}_c - \Omega_x^2 j^2 / 4\tau_0$ (Supplementary Information, section 4D). Here $\tilde{V}_c$ sets the barrier height with respect to μ (Fig. 1b, dashed black line), and $\Omega_x \ll \tau$ characterizes its curvature. We first consider the theoretical case of zero temperature, $\tilde{T} = k_B T$ (k_B, Boltzmann's constant), source–drain voltage, $\tilde{V}_{sd} = |e| V_{sd}$, and field, $\tilde{B}$: $\tilde{T} = \tilde{V}_{sd} = \tilde{B} = 0$. As $\tilde{V}_c$ is decreased below 0, the conductance, $g = G/G_Q$, increases from 0 to 1, showing a step of width $\sim\Omega_x$ (about 1.5 meV in our experiment), whose shape depends on U (Fig. 1k). In the upper part of the step, say $0.5 \lesssim g \lesssim 0.9$, we say that the QPC is 'sub-open'; the sub-open regime is of special interest because for measured $g(V_c)$ curves it contains the 0.7-anomaly.

The bare local density of states (LDOS), $A_j^0(\omega)$, for equation (1) has a strong maximum just above the band bottom[18], seen as a yellow–red ridge-like structure in Fig. 1b. In a semiclassical picture, $A_j^0(\omega) \propto 1/v_j(\omega)$, where $v_j(\omega)$ is the velocity at site j of an electron with energy ω with respect to μ. The ridge-like maximum of $A_j^0(\omega)$ above the barrier reflects the fact that electrons move slowest there. In the CCR's outer flanks, this ridge develops smoothly into the van Hove singularity, $A_{bulk}^0 \propto \left[(\omega - \omega_{bulk}^{min})\tau \right]^{-1/2}$, in the bulk LDOS at the bulk band bottom in the leads, $\omega_{bulk}^{min} = -\varepsilon_F$. We therefore call this LDOS structure a 'van Hove ridge'. Near the barrier's centre, its curvature causes the singularity to be smeared out on a scale set by Ω_x. This limits the amplitude of the van Hove ridge to $\max\left[A_j^0(\omega)\right] \propto \mathcal{O}(\Omega_x \tau_0)^{-1/2}$ and shifts it upwards in frequency relative to the band by $\mathcal{O}(\Omega_x)$ (Fig. 1f–h).

The van Hove ridge has a strong, $\tilde{V}_c$-dependent effect on numerous QPC properties. Near those spatial locations where the ridge intersects the chemical potential ($\omega = 0$), the LDOS is enhanced, thus amplifying the effects of interactions by $\mathcal{O}(\Omega_x \tau_0)^{-1/2}$ (which grows with QPC

[1]Center for NanoScience and Fakultät für Physik, Ludwig-Maximilians-Universität München, Geschwister-Scholl-Platz 1, 80539 München, Germany. [2]Arnold Sommerfeld Center for Theoretical Physics, Ludwig-Maximilians-Universität München, Theresienstrasse 37, D-80333 München, Germany. [3]Institut für Angewandte Physik, Universität Regensburg, D-93040 Regensburg, Germany. [4]Laboratory for Solid State Physics, ETH Zürich, CH-8093 Zürich, Switzerland.
*These authors contributed equally to this work.

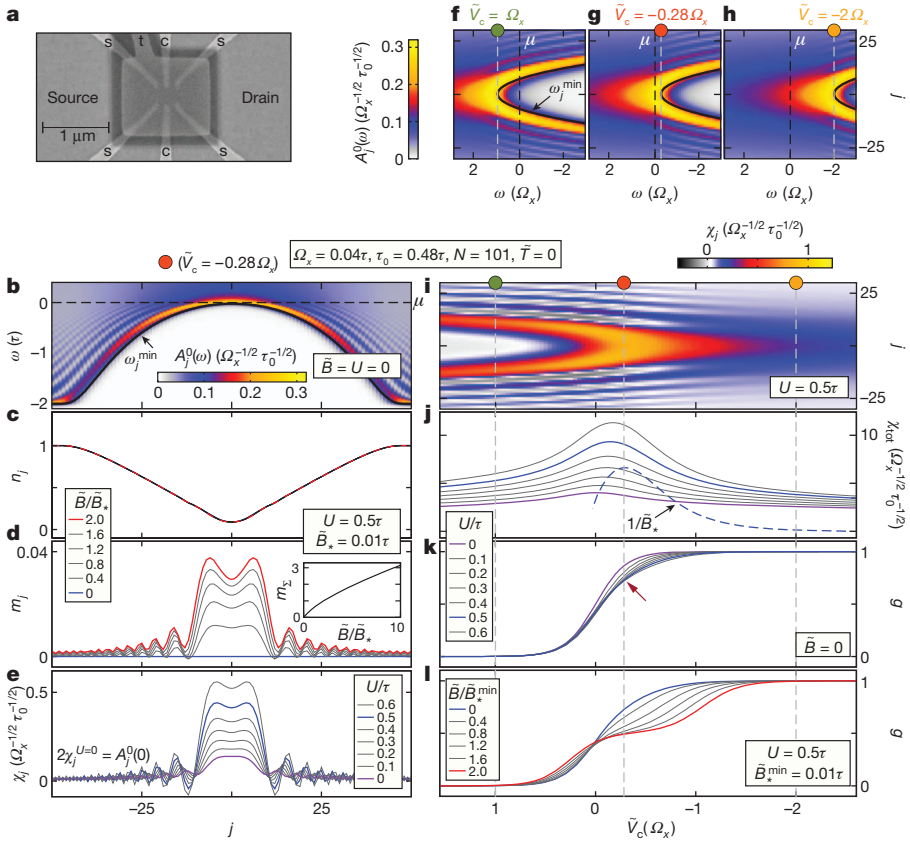

Figure 1 | Experimental set-up and model. **a**, Scanning electron microscope picture of the gate layout, featuring a top gate (t) at voltage V_t, two central gates (c) at voltage V_c and four side gates (s) at voltage V_s. Negative voltages V_c and V_s locally deplete the 2DES, which is 85 nm beneath the sample surface. Together with V_t, they induce a tunable electrostatic potential landscape in the 2DES. **b**, Barrier shape and LDOS. The bare ($U_j = 0$, $\tilde{B} = 0$) 1D LDOS per spin species, $A_j^0(\omega)$ (colour scale), as a function of energy, ω, and site index, j, for $\tilde{V}_c = -0.28\Omega_x$. The barrier shape is defined by the solid black line, showing the band bottom, ω_j^{min}. The LDOS vanishes exponentially rapidly below ω_j^{min} (Supplementary Fig. 11), and has a van Hove ridge (yellow–red) just above it, followed by Friedel oscillations (white fringes) at higher energies (up to $\omega \lesssim \tilde{V}_c$). **c**–**e**, Local properties of a sub-open QPC: FRG results for the sub-open barrier shown in **b**. **c**, **d**, The local density, n_j (**c**), and the magnetization, m_j (**d**), for several values of magnetic field, $\tilde{B}$. Inset of **d**, $m_\Sigma = \sum_{|j|\le 10} m_j$ as a function of $\tilde{B}$. **e**, The local spin susceptibility, χ_j, for several values of interaction strength, U. The shapes of m_j and χ_j are modulated by Friedel oscillations inherited from the bare LDOS (**b**), with locally varying wavelength, $\lambda \approx 1/n_j$. **f**–**l**, Changing barrier height. **f**–**h**, The bare LDOS, $A_j^0(\omega)$, for three successively lower barrier heights, $\tilde{V}_c/\Omega_x = 1$ (**f**), -0.28 (**g**) and -2 (**h**). The LDOS pattern is fixed with respect to $\tilde{V}_c$ (grey dashed lines) but shifts with respect to μ (black dashed lines). **i**–**l**, FRG results for the $\tilde{V}_c$ dependence of the local spin susceptibility, χ_j (colour scale), at fixed $U = 0.5\tau$ (**i**); the total spin susceptibility, $\chi_{tot} = \sum_j^{CCR} \chi_j$, for several U values (solid lines), and the inverse low-energy scale, $1/\tilde{B}_*$, for $U = 0.5\tau$ (dashed line) (**j**); the zero-temperature linear-response ($V_{sd} = 0$) conductance, $g = G/G_Q$, for several U values (at fixed $\tilde{B} = 0$) (**k**) and for several $\tilde{B}$ values (at fixed $U = 0.5\tau$) (**l**). For a large enough interaction, $U = 0.5\tau$, even for $\tilde{B} = \tilde{T} = \tilde{V}_{sd} = 0$ (blue lines in **k** and **l**), $g(\tilde{V}_c)$ has a shoulder (red arrow) at $g \approx 0.7$, the 0.7-anomaly. Three vertical dashed lines in **i**–**l** mark the three $\tilde{V}_c$ values used in **f**–**h**, as indicated by dots of matching colours.

length). In semiclassical terms, slow electrons feel interactions particularly strongly. When lowering the barrier top, $\tilde{V}_c$, to open the QPC, the van Hove ridge sweeps downwards (Fig. 1f–h); its interaction-amplifying effects are strongest in the $\tilde{V}_c$ regime where its apex, which has most weight, crosses μ. This happens for $0 \gtrsim \tilde{V}_c \gtrsim -\mathcal{O}(\Omega_x)$ (Fig. 1g), which, very importantly, encompasses the sub-open regime containing the 0.7-anomaly. Below, we show that the 0.7-anomaly and the zero-bias peak (ZBP) stem precisely from the amplification of interaction effects where the van Hove ridge intersects μ. The relevant implications are enhancements in the effective Hartree barrier governing elastic transmission, the spin susceptibility and the inelastic scattering rate, all of which lead to an anomalous reduction of g in the sub-open regime, especially for $T, B, V_{sd} > 0$.

Figure 1c–e illustrates several local properties, calculated at $\tilde{T} = 0$ using FRG, for the sub-open QPC barrier shown in Fig. 1b. We note four salient features, all intuitively expected. First, the local density, $n_j = \langle \hat{n}_{j\uparrow} + \hat{n}_{j\downarrow} \rangle$, is minimal at the barrier centre (Fig. 1c). Second, the local magnetization, $m_j = \langle \hat{n}_{j\uparrow} - \hat{n}_{j\downarrow} \rangle / 2$, vanishes at $B = 0$ (Fig. 1d, blue line); this reflects a physical assumption entailed in our calculations (Supplementary Information, section 6), namely that no spontaneous magnetization occurs, in contrast to the spontaneous spin splitting scenario advocated in refs 4, 8, 17. Third, m_j increases without saturation when $\tilde{B}$ becomes large (Fig. 1d, inset), indicating a smooth redistribution of spin, as expected for an open structure. Fourth, the local spin susceptibility, $\chi_j = (\partial m_j / \partial \tilde{B})_{\tilde{B}=0}$, is strongly enhanced with increasing U (Fig. 1e), because interactions amplify any field-induced spin imbalance.

The j dependence of χ_j is governed by that of $A_j^0(0)$ (in fact, $\chi_j^{U=0} = A_j^0(0)/2$), which is maximal near those sites where the van Hove ridge intersects μ. When $\tilde{V}_c$ is decreased through 0 (Figs 1f–h), these intersection points sweep out a parabolic arch in the $\tilde{V}_c - j$ plane, along which $\chi_j(\tilde{V}_c)$ (Fig. 1i, colour scale) is peaked, with most weight near the arch's apex. This leads to a corresponding peak in the total spin susceptibility, $\chi_{tot} = \sum_j^{CCR} \chi_j$, as a function of $\tilde{V}_c$ (Fig. 1j). This peak is strongly enhanced by increasing U (in accordance with the fourth feature above) and is located near the $\tilde{V}_c$ value where $g \approx 0.7$ (Fig. 1k). We will see further below that this peak strongly affects the $\tilde{B}$ dependence of the conductance (Fig. 1l).

Note that the spatial structure for $\chi_j(\tilde{V}_c)$ in Fig. 1i, namely two peaks merging into one as $\tilde{V}_c$ is lowered, is consistent with that, shown

in fig. 2b of ref. 14, for the density of spin-up electrons calculated using spin-density-functional theory, initialized in a small applied field to break spin symmetry. In ref. 14, the local maximum in the spin-up density was interpreted as evidence for a 'quasi-bound state' that was argued to host a spin-1/2 local moment; in contrast, features one and, especially, three above imply that our model yields no local moment.

Next we discuss the effect of the van Hove ridge on the conductance, $g(\tilde{V}_c)$, starting with its U dependence at $\tilde{B}=\tilde{T}=0$ (Fig. 1k). Increasing U skews the shape of the step in $g(\tilde{V}_c)$, which eventually develops a shoulder near $g\approx 0.7$ (red arrow). This shoulder develops because the increase in local density with decreasing $\tilde{V}_c$ is slightly nonlinear when the apex of the van Hove ridge drops past μ, causing a corresponding nonlinear upward shift in the effective Hartree barrier. For a parabolic barrier top, this occurs for $g\approx 0.7$. If the shape of the barrier top is changed to be non-parabolic, both the shape of the bare conductance step and the energy distance between the van Hove ridge apex and μ will change, which can cause the interaction-induced shoulder in g to shift away from 0.7. This explains the experimentally observed spread[6,12] of shoulders (that is, plateau values of the 0.7-anomaly) for $0.5 \lesssim g \lesssim 1$.

On increasing $\tilde{B}$ for fixed U and $\tilde{T}=0$ (Figs 1l and 2a), the shoulder in $g(\tilde{V}_c)$ becomes more pronounced, eventually developing into a spin-split plateau. Comparison of Fig. 2a with Fig. 2e shows that this development qualitatively agrees with experiment; the agreement was optimized by using U as fit parameter. Inspecting how the corresponding spin-resolved conductances, $g_\uparrow$ and $g_\downarrow$, change with $\tilde{B}$ (Fig. 2b), we note a strong asymmetry: although the bare barrier heights for spins $\uparrow$ and $\downarrow$ are shifted symmetrically by $-\tilde{B}/2$ and $\tilde{B}/2$, respectively, $g_\downarrow$ is decreased much more strongly than $g_\uparrow$ is increased. This is due to exchange interactions: increasing the spin-up density near the CCR centre (Fig. 1d) strongly raises the Hartree barrier, and more so for spin-down electrons than spin-up, owing to Pauli's exclusion principle. The consequences are most pronounced in the sub-open regime, owing to the van-Hove-ridge-induced peak in χ_{tot} there (Fig. 1j). We note, however, that $g_\uparrow = g_\downarrow$ at $\tilde{B}=0$, reflecting our above-mentioned assumption that no spontaneous spin splitting occurs.

Our FRG approach is limited to the case of zero temperature and zero source–drain voltage, for which no inelastic scattering occurs. To access qualitatively the effects of the latter at fixed U, we have instead used SOPT (Supplementary Information, section 7). Figure 2c–h shows a comparison of our SOPT results for the linear conductance, $g(\tilde{V}_c)$, calculated for several values of magnetic field, $\tilde{B}$, and temperature, $\tilde{T}=k_BT$, and our experimental data for $g(V_c)$. The measured conductance step shows a shoulder (Fig. 2e, f, red arrows) that becomes increasingly more pronounced with both increasing field, B (Fig. 2e), and increasing temperature, T (Fig. 2f), which is the hallmark of the 0.7-anomaly. Our perturbative calculations qualitatively reproduce both trends remarkably well. The only caveat is that the experimental curves in Fig. 2e, f show more pronounced shoulders than do the respective SOPT curves in Fig. 2c, d. This failure of SOPT to

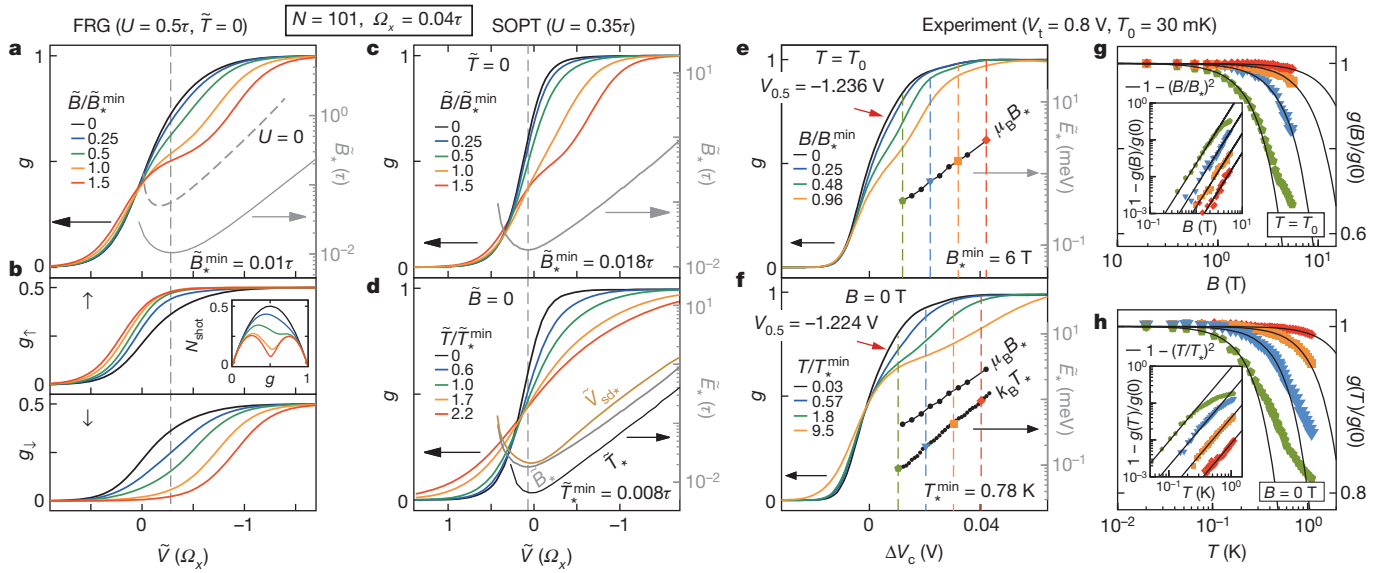

Figure 2 | Conductance: theory versus experiment. **a**, **b**, FRG results: the linear response conductance, $g(\tilde{V}_c, \tilde{B})$, of a QPC (**a**), and its spin-resolved components, $g_\uparrow$ and $g_\downarrow$ (**b**), plotted as functions of $\tilde{V}_c/\Omega_x$ for several values of $\tilde{B}$ at $\tilde{T}=0$ (but finite interaction U). The grey dashed and solid lines in **a** show the low-energy scale $\tilde{B}_*(\tilde{V}_c)$ for $U=0$ and $U=0.5$, respectively, plotted on the log-linear scale indicated on the right-hand axis (as also done in **c**–**f**). The small-field magnetoresponse in **a** is strongest when $\tilde{B}_*$ takes its smallest value, $\tilde{B}_*^{min}$ (vertical dashed lines). Inset of **b**, the shot noise factor, $N_{shot} = \sum_\sigma g_\sigma(1-g_\sigma)/2$, plotted as function of g. Its asymmetric development with $\tilde{B}$, which reflects that of $g_\uparrow$ and $g_\downarrow$, agrees qualitatively with experiment (see fig. 4d of ref. 7). **c**, **d**, SOPT results: $g(\tilde{V}_c, \tilde{B})$ at $\tilde{T}=0$ for several values of $\tilde{B}$ (**c**) and $g(\tilde{V}_c, \tilde{T})$ at $\tilde{B}=0$ for several values of $\tilde{T}$ (**d**), both plotted as functions of $\tilde{V}_c/\Omega_x$. The low-energy scale $\tilde{B}_*(\tilde{V}_c)$ is shown as a thin grey line in **c** and repeated in **d**; $\tilde{T}_*(\tilde{V}_c)$ and $\tilde{V}_{sd*}(\tilde{V}_c)$ are respectively shown as thin black and brown lines in **d**. The vertical dashed line indicates where $\tilde{B}_*$ takes its minimal value, $\tilde{B}_*^{min}$. For $\tilde{V}_c$ values below this dashed line, the lines for $\tilde{B}_*$, $\tilde{T}_*$ and $\tilde{V}_{sd*}$ in **d** are nearly straight on the log-linear scale, implying the behaviour summarized by equation (3), and are nearly parallel to each other, implying that the ratios $\tilde{B}_*/\tilde{T}_*$ and $\tilde{V}_{sd*}/\tilde{T}_*$ are essentially independent of $\tilde{V}_c$ there. **e**, **f**, Experiments—pinch-off curves. **e**, $g(V_c)$ measured at a low 2DES temperature, T_0, for various magnetic fields parallel to the 2DES, plotted as a function of $\Delta V_c = V_c - V_{0.5}$, where $V_{0.5}$ is the gate voltage for which the conductance at $B=0$ and $T=T_0$ is $g(V_{0.5})=0.5$. **f**, Analogous to **e**, but for $B=0$ and various temperatures T. Colours in **e** and **f** are chosen to provide comparability with theory curves in **a**, **c** and **d** (with the correspondence $|e|\Delta V_c \propto -\tilde{V}_c$). **g**, **h**, Experiments—Fermi-liquid behaviour: $g(B)/g(0)$ as function of B at temperature T_0 (**g**), and $g(T)/g(T_0)$ as function of T at $B=0$ (**h**), shown on log-linear scales (insets show their differences from unity on log-log scales) to emphasize small values of B and T. Coloured symbols distinguish data taken at different fixed V_c values, indicated by dashed lines of corresponding colour in **e** and **f**. The quadratic B and T dependences observed in **g** and **h** for each fixed V_c value confirm equation (2) and were used to determine the corresponding scales $B_*(V_c)$ and $T_*(V_c)$. (Black lines in **g** and **h** show $1-(B/B_*)^2$ and $1-(T/T_*)^2$, respectively.) The resulting energies, $E_* = \mu_B B_*(V_c)$ and $E_* = k_B T_*(V_c)$, are shown as functions of V_c in **e** (for B_*) and **f** (for both B_* and T_*) on a log-linear scale. The shape of these measured functions agrees qualitatively with the SOPT predictions in **c** and **d**, confirming the nearly exponential $\tilde{V}_c$ dependences and the nearly V_c-independent B_*/T_* ratio, discussed above. (For additional data, similar to that in **g** and **h**, see Supplementary Information, section 2B.)

produce real shoulders is present both in the low-field dependence at low temperature (compare Fig. 2e with Fig. 2c; the former, but not the latter, shows a weak shoulder even at zero field) and in the temperature dependence at zero field (compare Fig. 2f and Fig. 2d). In contrast, the more powerful FRG approach does reproduce the weak shoulder even for $\tilde{B}=\tilde{T}=0$, as discussed above; compare the black $g(\tilde{V}_c)$ curves in Fig. 2a (FRG) and Fig. 2c (SOPT). (That the latter curve, in contrast to the former, lies above its non-interacting version, $g^0(\tilde{V}_c)$, is an artefact of SOPT; see Supplementary Information, section 7D.)

We next focus on the limit of small energies $\tilde{B}$, $\tilde{T}$ and $\tilde{V}_{sd}$. Here our SOPT calculations yield three predictions, enumerated below, that are all consistent with our measurements. First, for fixed $\tilde{V}_c$, the leading dependence of the nonlinear conductance, $g_{nl}=(dI/d\tilde{V}_{sd})/G_Q$, on $\tilde{B}$, $\tilde{T}$ and $\tilde{V}_{sd}$ is predicted to be quadratic, as confirmed by the measured data in Figs 2g, h and 3a. This implies an expansion of the form

$$\frac{g_{nl}(\tilde{B},\,\tilde{T},\,\tilde{V}_{sd})}{g_{nl}(0,\,0,\,0)} \approx 1-\frac{\tilde{B}^2}{\tilde{B}_*^2}-\frac{\tilde{T}^2}{\tilde{T}_*^2}-\frac{\tilde{V}_{sd}^2}{\tilde{V}_{sd*}^2} \qquad (2)$$

for $\tilde{B}/\tilde{B}_*$, $\tilde{T}/\tilde{T}_*$, $\tilde{V}_{sd}/\tilde{V}_{sd*}\ll 1$, where $\tilde{B}_*$, $\tilde{T}_*$ and $\tilde{V}_{sd*}$ are $\tilde{V}_c$-dependent crossover scales that govern the 'strength' of the 0.7-anomaly for $U\neq 0$: the smaller these scales, the stronger the dependence on $\tilde{B}$, $\tilde{T}$ and $\tilde{V}_{sd}$ for a given $\tilde{V}_c$. Our SOPT results for these crossover scales are shown as thin lines on log-linear scales in Fig. 2c and Fig. 2d, respectively. Second, in that part of the sub-open regime where $g_{nl}(0,\,0,\,0)\approx 1$, they all depend exponentially on $\tilde{V}_c$:

$$\tilde{B}_*,\ \tilde{T}_*,\ \tilde{V}_{sd*} \propto \exp(-\pi\tilde{V}_c/\Omega_x) \qquad (3)$$

Third, and again for $g_{nl}(0,\,0,\,0)\approx 1$, the ratios $\tilde{B}_*/\tilde{T}_*$ and $\tilde{V}_{sd*}/\tilde{T}_*$ are essentially independent of $\tilde{V}_c$ (Supplementary Fig. 4). Remarkably, both the second and third predictions are confirmed by our experimental results (Fig. 2e for B_*, Fig. 2f for T_* and Supplementary Fig. 3 for V_{sd*}). The behaviour predicted by equation (3) for $\tilde{T}_*$ is also in accord with previous experiments[6] and with a perturbative treatment of interactions using Wentzel–Kramers–Brillouin wavefunctions[21]. Remarkably, the exponential $\tilde{V}_c$ dependence of the crossover scales stated in equation (3) can be understood from a non-interacting ($U=0$) theory, by using the bare transmission probability[3]

$$T_\sigma^0(\omega)=\left[e^{-2\pi(\omega-\tilde{V}_c+\sigma\tilde{B}/2)/\Omega_x}+1\right]^{-1} \qquad (4)$$

in the Landauer–Büttiker formula. A detailed analysis (Supplementary Information, section 5) shows that the crossover scales experience a further exponential reduction with increasing effective interaction strength, $U/\sqrt{\Omega_x\tau_0}$.

When plotted as a function of $\tilde{V}_c$, $1/\tilde{B}_*$ has a peak in the sub-open regime just before the onset of the exponential dependence of equation (3) (Fig. 1j). This peak is roughly similar in shape and position to that in $\chi_{tot}(\tilde{V}_c)$ (compare dashed and solid blue lines in Fig. 1j), except that the latter has a finite offset, reflecting the non-zero spin susceptibility of an open QPC. Thus, we predict, fourth, that $1/\tilde{B}_*$, which characterizes the strength of the low-field magnetoconductance, is roughly proportional to the spin susceptibility, χ_{tot}, of the CCR.

Next we address the remarkable experimental fact[6] that many low-energy properties of the 0.7-anomaly (including our first and third predictions) are similar to those seen in transport through a Kondo quantum dot (KQD). This led to the proposal[13,14] that a QPC harbours

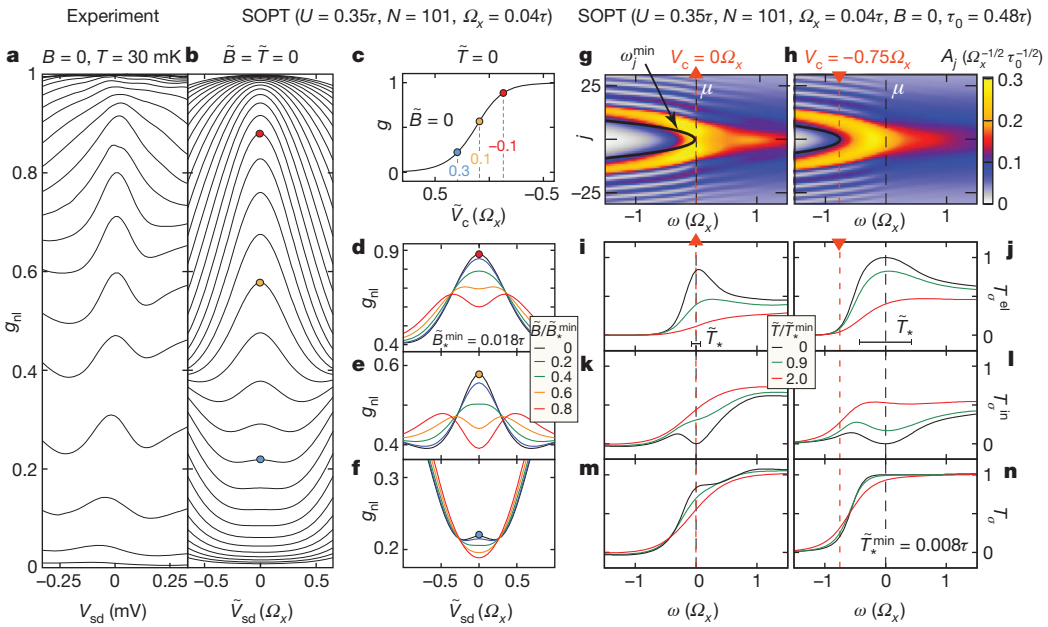

Figure 3 | Finite excitation energies. **a**–**f**, Zero-bias peak. **a**, Experimental data for the nonlinear conductance, g_{nl}, as a function of source–drain voltage, measured for several V_c values at a fixed low temperature and zero field. **b**, Keldysh SOPT results for $g_{nl}(\tilde{V}_{sd})$ for several $\tilde{V}_c$ values at $\tilde{T}=\tilde{B}=0$, showing qualitative agreement with **a**. **c**, The linear-response conductance, $g=g_{nl}(\tilde{V}_{sd}=0)$, as a function of $\tilde{V}_c$. **d**–**f**, $g_{nl}(\tilde{V}_{sd})$ as in **b**, but for three different $\tilde{V}_c$ values (compare colour-matched dots in **c** and **b**) and five different magnetic field values in each panel. Increasing $\tilde{B}$ causes the ZBP to split into two subpeaks once $\tilde{B}\gtrsim\tilde{B}_*$; the splitting is therefore most pronounced in **e**, for which $\tilde{B}_*$ is smallest. A detailed discussion of the ZBP, including its T dependence, will be published elsewhere. Here we would like to point out the qualitative agreement of **d**–**f** with published data; see, for example, fig. 2d of ref. 6. **g**, **h**, Interacting LDOS: $A_j(\omega)$, calculated using SOPT, shown for two fixed gate voltage values, $\tilde{V}_c/\Omega_x=0$ (**g**) and -0.75 (**h**) (red dashed lines). **i**–**n**, Equilibrium transmission probabilities: the corresponding elastic, inelastic and total transmission probabilities, T_σ^{el} (**i**, **j**), T_σ^{in} (**k**, **l**) and T_σ (**m**, **n**), calculated using SOPT and shown as functions of energy, ω, for three different temperatures. At $\tilde{T}=0$ (black curves) $T_\sigma^{in}(\omega)$ vanishes at $\omega=0$, where there is no phase space for inelastic scattering. However, it increases as ω changes from zero, causing a corresponding reduction in the elastic transmission for $\omega\neq 0$, such that $T_\sigma^{el}(\omega)$ has a narrow 'low-energy peak' around $\omega=0$. On increasing the temperature, the probability of inelastic scattering increases, causing the minimum in $T_\sigma^{in}(\omega)$ and the peak in $T_\sigma^{el}(\omega)$ to be smeared out. This leads to a net $\tilde{T}$-induced reduction in the total transmission, $T_\sigma(\omega)$ near $\omega=0$, causing a corresponding reduction in the conductance (Fig. 2d, f). This reduction is stronger for $\tilde{V}_c/\Omega_x=0$ (**m**) than for $\tilde{V}_c/\Omega_x=-0.75$ (**n**), because the probability of electron–hole pair creation during inelastic scattering is largest when apex of the van Hove ridge lies closest to μ (compare **g** and **h**).

a quasi-bound state, whose local moment gives rise to the Kondo effect. In contrast, our van-Hove-ridge scenario fully explains the 0.7-anomaly without invoking the Kondo effect. In particular, we find no indications that a smooth parabolic barrier hosts a discrete, localized spin (compare with the third feature above), and no Kondo effect/0.7-anomaly similarities (experimentally or theoretically) at high energies ($\gtrsim \tilde{B}_*$), where the Kondo effect is governed by an unscreened local moment. Nevertheless, the two phenomena do have similar low-energy behaviour. This is because both involve a spin-singlet ground state featuring spatially confined spin fluctuations. For a KQD they result from screening of the localized spin, whereas for a QPC they result from the extended structure of the van Hove ridge (Fig. 1i); but this distinction, which is important on short length scales (high energies), does not matter on long ones (low energies). These spin fluctuations are characterized by exponentially small energy scales, the Kondo temperature for a KQD, and $\tilde{T}_*$ for a QPC, both scaling inversely with the local spin susceptibility (for a QPC, this follows from prediction four). For a KQD, the local spin fluctuations can be described by Nozières–Fermi-liquid theory[27,28] in terms of scattering phase shifts, which determine its low-energy properties. Because a QPC, like a KQD, harbours spatially confined spin fluctuations, a similar Nozières–Fermi-liquid framework applies, explaining why its low-energy transport properties are similar to those of a KQD.

We next study finite excitation energies ($\tilde{T}$, $\tilde{V}_{sd} > 0$), where inelastic scattering becomes important (Fig. 3). We begin by considering the nonlinear differential conductance, g_{nl}, as a function of source–drain voltage, V_{sd}. Experimentally, g_{nl} shows a narrow peak at $V_{sd} = 0$ (Fig. 3a; see also refs 6, 9, 10). This ZBP appears strongest in the sub-open regime, but remains visible even very close to pinch off[10] ($g \to 0$). It splits with increasing field once B exceeds a V_c-dependent crossover value that is smallest when $g \approx 0.7$ (see fig. 2d of ref. 6). Remarkably, our model, treated using Keldysh SOPT (Supplementary Information, section 7B), yields a ZBP (Fig. 3b, d–f) that qualitatively reproduces this behaviour. In the sub-open regime ($0.5 \lesssim g \lesssim 0.9$), a ZBP arises even without interaction (this follows from equation (4)), but interactions modify it in two ways (Supplementary Information, section 7C): a finite V_{sd} causes a net charge enhancement at the barrier, resulting in a reduction of transmission due to Coulomb repulsion; and opens up a finite phase space for inelastic backscattering. Both effects strongly depend on the LDOS near μ (Fig. 3g, h), and are thus strongest when the apex of the van Hove ridge lies near μ (as in Figs 3g and 1g). However, the van Hove ridge intersects μ also for $g < 0.5$ (as in Fig. 1f), which explains why a ZBP is experimentally observed even close to pinch off[10].

The two modification mechanisms just discussed also apply to the case of increasing temperature. To highlight the role of inelastic scattering, we now discuss (for $\tilde{B} = \tilde{V}_{sd} = 0$) the transmission probability $T_\sigma(\omega) = T_\sigma^{el}(\omega) + T_\sigma^{in}(\omega)$, written as the sum of elastic and inelastic contributions corresponding respectively to transmission without or with the creation of electron–hole pairs (see Supplementary Information, section 7A, for their precise definition). Figure 3i–n shows examples of these quantities. With increasing temperature, the probability for inelastic scattering increases, causing $T_\sigma^{in}(\omega)$ to increase (Fig. 3k, l) and $T_\sigma^{el}(\omega)$ to decrease (Fig. 3i, j). This leads to a net temperature-induced reduction in the total transmission, $T_\sigma(\omega)$ (Fig. 3m, n), near $\omega = 0$, causing a corresponding reduction in the conductance (Fig. 2d, f). Importantly, this reduction is V_c dependent: it is strongest when the apex of the van Hove ridge lies near μ (as in Fig. 3m) and decreases away from this point (as in Fig. 3n), because the probability for electron–hole pair creation during inelastic scattering increases with the LDOS near μ. The fact that $T_\sigma(\omega)$ acquires a non-trivial, interaction-induced dependence on $\tilde{T}$ in the sub-open regime is consistent with the fact that near $g \approx 0.7$ the measured thermopower violates the Mott relation[5], which is based on the assumption of non-interacting electrons.

Finally, we note that we have studied the magnetic field dependence of the transconductance, dG/dV_c, both experimentally and by using FRG. We obtain excellent qualitative agreement between experiment and theory, showing that such measurements can be understood without invoking spontaneous spin polarization, as is often advocated to explain them[4,8,17]. A detailed analysis (Supplementary Information, section 2C, and Supplementary Fig. 5) establishes that the g factor is enhanced significantly by interactions, and that interaction strength can be tuned experimentally using a top gate.

We have presented detailed microscopic calculations that qualitatively reproduce the full phenomenology of the 0.7-anomaly. We argued that a van Hove ridge in the LDOS, combined with interactions, provides a natural explanation for the anomalous behaviour of the conductance of a sub-open ($g \gtrsim 0.5$) QPC. The experimentally observed[6] similarities between the 0.7-anomaly and the Kondo effect at low energies arise because both phenomena involve spatially localized spin fluctuations; at high energies, the similarities cease. We verified our Fermi-liquid predictions for the QPC conductance by systematic measurement of the conductance as a function of V_c, B and T. Strikingly, we demonstrated that the zero-bias peak in a QPC arises from the interplay of interactions and geometry. By implication, anomalous zero-bias behaviour might also arise in other systems involving interacting electrons traversing 1D low-density regions with slowly varying spatial inhomogeneities, such as the gated nanowires being studied in the search for Majorana fermions[29].

METHODS SUMMARY

The nanostructure is laterally defined in a 2DES located 85 nm beneath the surface of a GaAs/AlGaAs heterostructure. The low-temperature carrier density and mobility are $1.9 \times 10^{11}\,cm^{-2}$ and $1.2 \times 10^6\,cm^2\,V^{-1}\,s^{-1}$, respectively. Electron-beam lithography was used to create the Ti/Au gates. The top gate is electrically insulated from the others by cross-linked poly(methyl methacrylate). Perfect alignment of magnetic fields parallel to the 2DES and the 1D channel defining the QPC was ensured by using a two-axis magnet and was controlled by magnetotransport measurements. We used a dilution refrigerator and reached electron temperatures as low as $T_{2DES} \approx 30$ mK.

Our most accurate theoretical results were obtained by using FRG[24–26] to calculate $T = 0$ properties. FRG amounts to doing renormalization-group-enhanced perturbation theory in the interaction U. In setting up our FRG flow equations, we made two approximations, both exact to second order in U: we truncated the infinite hierarchy of flow equations by neglecting the flow of the three-particle vertex; and we set to zero all components of the two-particle vertex that are not already generated to second order in the interaction (coupled-ladder approximation).

To access the effects of inelastic scattering for $\tilde{T} > 0$ or $\tilde{V}_{sd} > 0$ at fixed U, we used SOPT: we dressed bare Green's functions by evaluating the self-energy perturbatively to second order in the interaction. For $\tilde{V}_{sd} = 0$, we calculated the linear conductance following the strategy in ref. 23, generalized to $\tilde{B} \neq 0$ and broken electron–hole symmetry. For $\tilde{V}_{sd} > 0$, we calculated the nonlinear conductance, $g_{nl} = (dI/d\tilde{V}_{sd})/G_Q$, using the Meir–Wingreen formula for the current (equation (6) of ref. 30).

Received 16 November 2012; accepted 26 June 2013.
Published online 28 August 2013.

1. van Wees, B. J. *et al.* Quantized conductance of point contacts in a two-dimensional electron gas. *Phys. Rev. Lett.* **60,** 848–850 (1988).
2. Wharam, D. A. *et al.* One-dimensional transport and the quantisation of the ballistic resistance. *J. Phys. C* **21,** L209–L214 (1988).
3. Büttiker, M. Quantized transmission of a saddle-point constriction. *Phys. Rev. B* **41,** 7906(R) (1990).
4. Thomas, K. J. *et al.* Possible spin polarization in a one-dimensional electron gas. *Phys. Rev. Lett.* **77,** 135–138 (1996).
5. Appleyard, N. J. *et al.* Direction-resolved transport and possible many-body effects in one-dimensional thermopower. *Phys. Rev. B* **62,** R16275–R16278 (2000).
6. Cronenwett, S. M. *et al.* Low-temperature fate of the 0.7 structure in a point contact: a Kondo-like correlated state in an open system. *Phys. Rev. Lett.* **88,** 226805 (2002).
7. DiCarlo, L. *et al.* Shot-noise signatures of 0.7 structure and spin in a quantum point contact. *Phys. Rev. Lett.* **97,** 036810 (2006).
8. Koop, E. J. *et al.* The influence of device geometry on many-body effects in quantum point contacts: signatures of the 0.7-anomaly, exchange and Kondo. *J. Supercond. Nov. Magn.* **20,** 433–441 (2007).
9. Sarkozy, S. *et al.* Zero-bias anomaly in quantum wires. *Phys. Rev. B* **79,** 161307R (2009).
10. Ren, Y. *et al.* Zero-bias anomaly of quantum point contacts in the low-conductance limit. *Phys. Rev. B* **82,** 045313 (2010).

11. Micolich, A. P. What lurks below the last plateau: experimental studies of the $0.7 \times 2e^2/h$ conductance anomaly in one-dimensional systems. *J. Phys. Condens. Matter* **23,** 443201 (2011).
12. Burke, A. *et al.* Extreme sensitivity of the spin-splitting and 0.7 anomaly to confining potential in one-dimensional nanoelectronic devices. *Nano Lett.* **12,** 4495–4502 (2012).
13. Meir, Y., Hirose, K. & Wingreen, N. S. Kondo model for the 0.7 anomaly in transport through a quantum point contact. *Phys. Rev. Lett.* **89,** 196802 (2002).
14. Rejec, T. & Meir, Y. Magnetic impurity formation in quantum point contacts. *Nature* **442,** 900–903 (2006).
15. Ihnatsenka, S. & Zozoulenko, I. V. Conductance of a quantum point contact based on spin density-functional theory. *Phys. Rev. B* **76,** 045338 (2007).
16. Matveev, K. A. Conductance of a quantum wire at low electron density. *Phys. Rev. B* **70,** 245319 (2004).
17. Reilly, D. J. Phenomenological model for the 0.7 conductance feature in quantum wires. *Phys. Rev. B* **72,** 033309 (2005).
18. Sloggett, C. Milstein, A. I. & Sushkov, O. P. Correlated electron current and temperature dependence of the conductance of a quantum point contact. *Eur. Phys. J. B* **61,** 427–432 (2008).
19. Aryanpour, K. & Han, J. E. Ferromagnetic spin coupling as the origin of 0.7 anomaly in quantum point contacts. *Phys. Rev. Lett.* **102,** 056805 (2009).
20. Güçlü, A. D. *et al.* Localization in an inhomogeneous quantum wire. *Phys. Rev. B* **80,** 201302(R) (2009).
21. Lunde, A. M. *et al.* Electron-electron interaction effects in quantum point contacts. *New J. Phys.* **11,** 023031 (2009).
22. Goldhaber-Gordon, D. *et al.* Kondo effect in a single-electron transistor. *Nature* **391,** 156–159 (1998).
23. Oguri, A. Transmission probability for interacting electrons connected to reservoirs. *J. Phys. Soc. Jpn* **70,** 2666–2681 (2001).
24. Andergassen, S. *et al.* Renormalization-group analysis of the one-dimensional extended Hubbard model with a single impurity. *Phys. Rev. B* **73,** 045125 (2006).
25. Karrasch, C., Enss, T. & Meden, V. Functional renormalization group approach to transport through correlated quantum dots. *Phys. Rev. B* **73,** 235337 (2006).
26. Metzner, W. *et al.* Functional renormalization group approach to correlated fermion systems. *Rev. Mod. Phys.* **84,** 299–352 (2012).
27. Nozières, P. A ''fermi-liquid'' description of the Kondo problem at low temperatures. *J. Low Temp. Phys.* **17,** 31–42 (1974).
28. Glazman, L&. Pustilnik, M. in *Nanophysics: Coherence and Transport* (eds Bouchiat, H. *et al.*) 427–478 (Elsevier, 2005).
29. Mourik, V. *et al.* Signatures of Majorana fermions in hybrid superconductor-semiconductor nanowire devices. *Science* **336,** 1003–1007 (2012).
30. Meir, Y. & Wingreen, N. S. Landauer formula for the current through an interacting electron region. *Phys. Rev. Lett.* **68,** 2512–2515 (1992).

Supplementary Information is available in the online version of the paper.

Acknowledgements We thank B. Altshuler, P. Brouwer, R. Egger, J. Folk, L. Glazman, V. Golovach, A. Hamilton, A. Högele, Y. Imry, M. Kiselev, J. Kotthaus, D. Logan, D. Loss, C. Marcus, Y. Meir, H. Monien, M. Pepper, M. Pustilnik, A. Rosch, K. Schönhammer, B. Spivak and A. Yacoby for discussions, and, in particular, S. Andergassen, C. Honerkamp, S. Jakobs, C. Karrasch, V. Meden, M. Pletyukhov and H. Schoeller for FRG-related help and advice. We acknowledge support from the DFG through SFB-631, SFB-TR12, De730/3-2, De730/4-1, De730/4-2, De730/4-3, HO 4687/1-3, LU819/4-1 and the Cluster of Excellence Nanosystems Initiative Munich; from the Center for NanoScience; and from the US National Science Foundation under grant no. NSF PHY05-51164. S.L. acknowledges support through a Heisenberg fellowship of the DFG.

Author Contributions J.v.D. and S.L. coordinated the project: J.v.D. initiated and supervised the theoretical work, and S.L. planned and supervised the experiments and their analysis. F.B. and J.H. carried out the calculations using FRG, and J.H., F.B. and B.B. carried out the calculations using perturbation theory. D.S. and W.W. provided the wafer material, and D.B. fabricated the nanostructure. E.S., D.B., D.T. and S.L. carried out the measurements, and E.S., D.B., F.B. and J.H. carried out the experimental data analysis. J.H. and F.B. prepared the figures, and J.v.D., S.L., F.B., J.H. and E.S. wrote the paper.

Author Information Reprints and permissions information is available at www.nature.com/reprints. The authors declare no competing financial interests. Readers are welcome to comment on the online version of the paper. Correspondence and requests for materials should be addressed to J.v.D. (vondelft@lmu.de) or S.L. (ludwig@lmu.de).